Models to Incorporate Reaction Mechanisms into DG-OSPREY:

Fixed-Bed Simulations for Organic Iodides Capture Using Ag^0Z

Annual Report for Project DE-NE0008761, Capture of Organic Iodides from Vessel Off-Gas Streams

Project Number: 18-15596
Project Period: October 1, 2018 - September 30, 2022

Ziheng Shen
Alexander I. Wiechert
Austin P. Ladshaw
Sotira Yiacoumi (Co-PI)
School of Civil and Environmental Engineering
Georgia Institute of Technology

Costas Tsouris (Co-PI)
Oak Ridge National Laboratory

Submission date: September 30, 2022

Executive Summary

As one of the most potent radioisotopes released during spent nuclear fuel reprocessing, ^{129}I is strictly regulated and must be removed before discharge. Organic iodides (primarily alkyl iodides with different chain lengths, i.e., CH_3I, C_4H_9I, and $C_{12}H_{25}I$) comprise ~2% of the total iodine in the reprocessing off-gases and are primarily present in vessel off-gas (VOG). Reduced silver mordenite (Ag^0Z) is predominantly considered for the removal of radioiodine; however, its capture performance and underlying interaction processes with long-chain organic iodides are not fully understood. Two major tasks were accomplished in this study. First, to improve upon the previous experimental studies where Ag^0Z was used to capture CH_3I, C_4H_9I, and $C_{12}H_{25}I$ at different concentrations, we comprehensively investigated the corresponding capture mechanisms by characterizing fully loaded Ag^0Z samples. Second, computational codes were implemented to perform fixed-bed simulations that account for transport and reaction mechanisms.

Scanning electron microscopy with energy dispersive X-ray analysis (SEM-EDX), powder X-ray diffraction (PXRD), UV-visible diffuse reflectance spectroscopy (UV-vis DRS), and thermogravimetric analysis (TGA) were conducted on Ag^0Z samples that are saturated with I_2, CH_3I, C_4H_9I, and $C_{12}H_{25}I$, respectively. Results indicate that AgI is the predominant adsorption product regardless of the adsorbed iodine species, yet alkyl iodides with different carbon chain lengths may have different compositions of α- and γ-AgI. Synchrotron pair distribution function (PDF) measurements and TGA coupled with a Fourier transformed infrared detector (TGA-FTIR) have been performed, and experimental data are currently analyzed. Results are expected to provide further insights into the adsorption mechanisms.

The fixed-bed capture performance for CH_3I was successfully simulated by solving mathematical equations that describe the underlying transport processes and adsorption reactions. The computational framework, Catalytic After Treatment System (CATS), that was originated in our research group, was used to solve the governing equations. Kinetic parameters, including the pore diffusivity and reaction rate constant were obtained by optimization techniques using data from thin-bed experiments performed at Oak Ridge National Laboratory. The performance of a deep bed predicted using the optimized parameters showed promising agreement with the experimental data.

Part 1: Investigating the Mechanisms of Long-chain Organic Iodides Adsorption on Ag^0Z

Key Personnel

Ziheng Shen (Ph.D. Student), Alexander Wiechert (Postdoc), Austin Ladshaw (Former Ph.D. Student), Costas Tsouris (Co-PI), Sotira Yiacoumi (PI)

1.1 Scope

In a reprocessing facility, it is generally acknowledged that over 90% of the iodine is volatilized to the dissolver off-gas (DOG) stream during the dissolution step and is primarily present as I_2. Around 2% of the total iodine inventory is, nevertheless, released in vessel off-gas (VOG) as complex organic iodides (primarily alkyl iodides with different chain lengths, i.e., CH_3I, C_4H_9I, and $C_{12}H_{25}I$), as a result of reactions between I_2 and carbon-based components in nuclear power plants (e.g., epoxy).[1, 2] Although these organic iodides are at lower concentrations than I_2, they must also be captured before discharging.

Since the 2000s, particularly after the Fukushima accident in 2011, increasing emphasis has been placed on the capture of organic iodides. Researchers from multiple U.S. national laboratories and universities have performed systematic studies on organic iodides capture. Particular attention has been attracted for Ag^0Z, the baseline material that has a high Ag content and promising stability in acidic waste streams.[3] Various experiments including thin-bed and deep-bed tests were conducted to evaluate the capture performance for CH_3I using Ag^0Z at different operating conditions (concentrations, temperature, carrier gas, etc.).[4] Furthermore, mechanistic studies for CH_3I adsorption were also performed. For instance, Nenoff et al. analyzed Ag^0Z capturing CH_3I in a complex gas stream (containing NO_x and H_2O), in which they proposed that CH_3I decomposes to surface methoxy species that eventually form methanol and dimethyl ether, and the liberated iodine reacts with Ag within the mordenite pores yielding sub-nanometer α-AgI. A similar catalytic decomposition of CH_3I, in a dry air carrier gas, was also identified for adsorption using Ag-faujasite by Chebbi et al. through a series of *in situ* characterization. These investigations are, nevertheless, very limited for organic iodides with longer chain length.

1.2 Experimental Methods

Iodine loading experiments were performed by the team at Oak Ridge National Laboratory. Specifically, the Ag^0Z pellets were packed one at a time as a thin bed (1-3 pellets in depth) onto a sample holding plate.[5] Before I_2 loading, the Ag^0Z samples were first dried for 24h at 150ºC in a stream of compressed dry air (dew point <−70 ˚C) to remove excess physisorbed water. After that, a dry air gas stream containing one of four prototypical iodine species present in reprocessing off gas, i.e., I_2, CH_3I, iodobutane (C_4H_9I), or iododododecane ($C_{12}H_{25}I$), at a concentration of ~50 ppmv and a temperature of 150 ºC was introduced. The detailed experimental procedures and results have been reported by Greaney et al.[5] The unreduced AgZ, Ag^0Z, and iodine loaded Ag^0Z pellets were stored in opaque bottles and sent to Georgia Tech for further characterization.

The Ag^0Z pellets were ground into fine powders for characterization. The techniques utilized included scanning electron microscopy with energy dispersive X-ray analysis (SEM-EDX),

powder X-ray diffraction (PXRD), UV-visible diffuse reflectance spectroscopy (UV-vis DRS), and thermogravimetric analysis (TGA).

1.3 Experimental Results

1.3.1 Iodine Loading Experiments

The results for the thin-bed iodine loading experiments have been reported by Greaney et al.[5] Specifically, the iodine loading curves and saturated iodine capacities for each organic iodide species are presented in Figure 1a and Table 1, respectively. At equilibrium, all samples displayed similar iodine capacities (100 ± 10 mg I/g Ag^0Z) though the loading rates differed. A distinct difference was observed at the initial stage of loading, in which the uptake rate can be ranked as I_2 > $C_{12}H_{25}I$ ≈ C_4H_9I > CH_3I. One thing worth noting is that the $C_{12}H_{25}I$ loaded Ag^0Z has a unique color that sets it apart from the other samples after saturation is reached (Figure 1b), which implies that the long-chain alkyl iodides may have different mechanisms of adsorption. In previous studies, a series of visual examinations were performed and a shrinking-core process in the iodine-loaded pellets was observed.[5] A comprehensive investigation on the physical and chemical properties has, nonetheless, not been conducted.

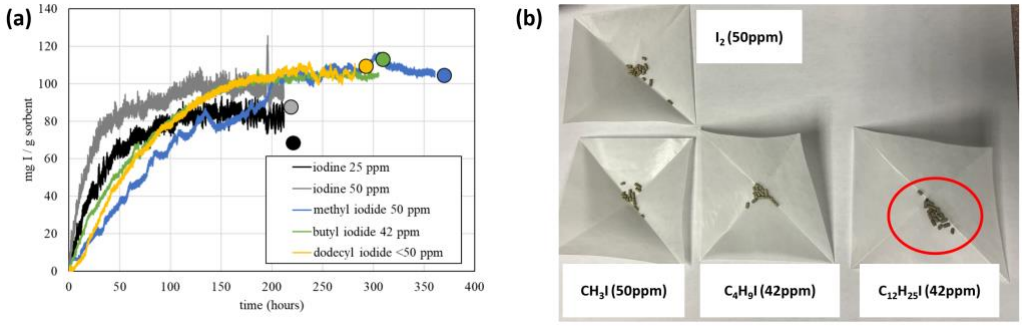

Figure 1. (a) ~50 ppmv CH_3I, C_4H_9I, $C_{12}H_{25}I$, and I_2 loading curves for Ag^0Z.[5] (b) Pictures of Ag^0Z fully loaded with different iodine species; the $C_{12}H_{25}I$ loaded sample displayed a darker green color which sets it apart from the others.

Table 1. Iodine capacities for Ag^0Z loaded with I_2 and organic iodides; the capacities were measured by a thermogravimetric analyzer (TGA) and neutron activation analysis (NAA).[5]

Gas species	Conc	TGA (mg I/g sorbent)	NAA (mg I/g sorbent)
I_2	50ppmv	100	85.5+-8.6
CH_3I	50ppmv	111	106.6+-10.7
C_4H_9I	42ppmv	104	114.8+-11.5
$C_{12}H_{25}I$	<=50ppmv	110	112.0+-11.2

1.3.2 Sample Characterization

1.3.2.1 SEM-EDX Analysis

SEM-EDX was first performed to examine the surface of unreduced AgZ (Figure 2a), Ag^0Z (Figure 2b), and Ag^0Z samples loaded with different iodine species (Figures 2c-f). The SEM images show that surface morphology did not have significant variation in all the samples, and

all exhibit irregular rough surfaces with small particulates distributed evenly. The EDX mapping results for Ag (for all samples) and I (for iodine loaded samples) were also listed. Compared to the AgZ sample which showed a homogeneous distribution of Ag (Figure 2a), the Ag^0Z sample displayed distinct concentrated regions of Ag (Figure 2b). These concentrated Ag regions essentially represent Ag nanoparticles (at sizes of several nanometers to micrometers) generated during the reduction process. After loaded with iodine, Ag is distributed uniformly on most of the surface, while some concentrated regions also exist sparsely. The I mapping results mostly overlap with the Ag ones, suggesting that Ag and I follow the same distributions on the surface of each material. This observation implies that AgI is likely the final adsorption product for all the iodine-loaded samples. Some of the AgI may aggregate into large particles resulting in concentrated regions on the map, whereas the remaining exists as small nanoparticles on the surface or, potentially, as α-AgI anchored within mordenite channels. This phenomenon is consistent among all the iodine loaded samples regardless of the adsorbed species, implying that there are few, if any, differences in the adsorption products for organic iodides with different chain lengths.

1.3.2.2 PXRD and UV-vis DRS

PXRD and UV-vis DRS were conducted to further evaluate the properties of Ag^0Z loaded with different iodine species. For the PXRD results (Figure 3a), crystalline Ag^0 patterns are observed in Ag^0Z samples but are absent in AgZ samples, reinforcing the successful installation of Ag^0 nanoparticles during the reduction of commercial AgZ. The iodine-loaded samples did not exhibit observable differences in the crystalline structures, and γ-AgI was consistently the major adsorption product (Figure 3a). Ag^0 patterns barely persist in all iodine loaded Ag^0Z samples, which suggests that most crystalline Ag^0 was utilized during the adsorption processes.

UV-vis DRS was conducted to examine the Ag speciation (oxidation state) in the samples. In addition to AgZ, Ag^0Z, and iodine loaded Ag^0Z samples, commercial AgI powder was also analyzed as a standard chemical (Figure 3b). The assignment of UV-vis bands for Ag-zeolites has been well established. The unreduced Ag^+Z exhibited two distinct bands at 206 and 256 nm, representing Ag^+ located at mordenite exchange sites and cationic charged Ag in the form of small clusters ($Ag^{\delta+}$), respectively.[6] These two bands persist after reduction to Ag^0Z whilst two new bands at 323 and 380 nm emerged. The former may be referred to as $Ag^{\delta+}$ at larger cluster size but didn't exhibit metallic properties, and the latter is well documented as a representation of Ag^0 nanoparticles.[7] All of the iodine loaded samples showed an absorption edge at around 430 nm, which represents AgI. The position of this edge for iodine loaded Ag^0Z is, however, slightly lower than that of a standard AgI powder. Such blueshift may be an indication that the AgI nanoparticles formed during adsorption are smaller in size than those in the standard AgI chemical.[6] The spectra for I_2-, CH_3I-, C_4H_9I- loaded Ag^0Z mostly overlap, while the $C_{12}H_{25}I$-loaded sample showed an intense tail above the AgI absorption edge. Since AgZ displays negligible absorption beyond 400 nm, the tail observed in the $C_{12}H_{25}I$-loaded sample is not a result from the mordenite backbone. This result may, reasonably, imply that some Ag^0 nanoparticles in the $C_{12}H_{25}I$-exposed Ag^0Z remained after saturation, while no Ag^0 nanoparticles persisted in other iodine-loaded samples. Given that PXRD does not show distinct Ag^0 patterns for $C_{12}H_{25}I$-loaded Ag^0Z, these Ag^0 nanoparticles, if existed, should be very small in size. Such observation may, alternatively, be explained by the formation of other potential products which must be further assessed by other characterization methods.

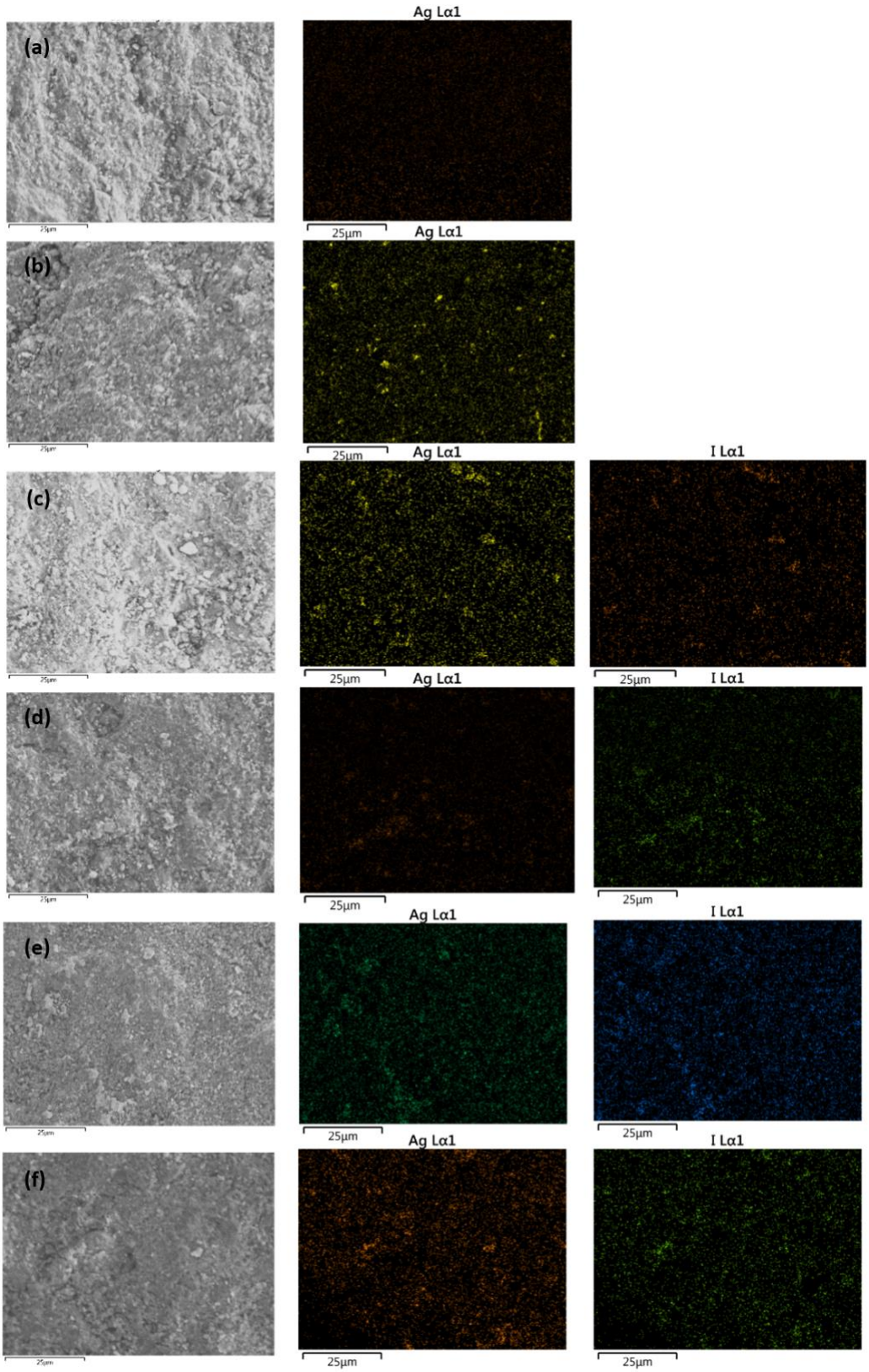

Figure 2. SEM images and EDX mapping results for (a) unreduced AgZ, (b) reduced Ag^0Z, (c) I_2 -loaded Ag^0Z, (d) CH_3I -loaded Ag^0Z, (e) C_4H_9I -loaded Ag^0Z, and (f) $C_{12}H_{25}I$ -loaded Ag^0Z.

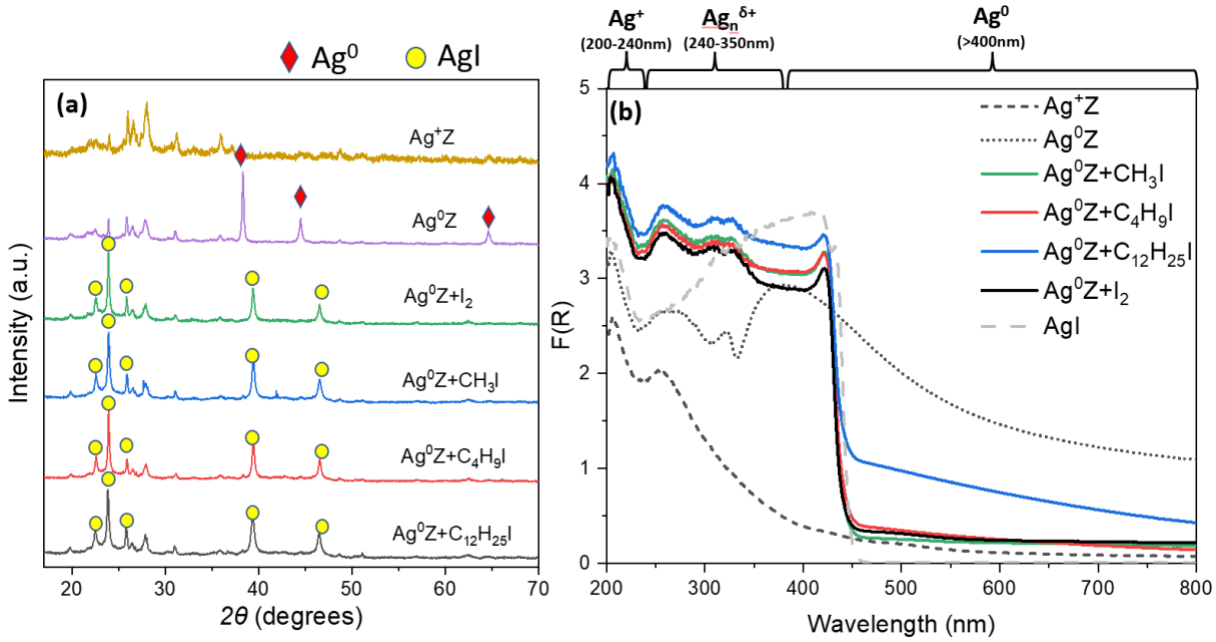

Figure 3. (a) PXRD and (b) UV-vis DRS for AgZ, Ag^0Z, and CH_3I, C_4H_9I, $C_{12}H_{25}I$, and I_2 loaded Ag^0Z (the UV-Vis DRS for standard AgI is also included).

1.3.2.3 Thermal Analysis

TGA was performed to assess the thermal stability and content of volatile compounds in each sample (Figure 4). A weight loss of ~7% before 350°C can be attributed to H_2O or trace CO_2 that physisorbed on the mordenite surface or within the channels. The mass change of the Ag^0Z sample reached equilibrium at ~450°C (7.45% weight loss) indicating that little, if any, amount of volatile species was sustained at this temperature. An extra 2.6-3.9% of mass loss was observed after 350°C in iodine loaded samples compared to pristine Ag^0Z. This mass loss is predominantly attributed volatile I^- that has been reported previously.[8] The onset temperatures (i.e., the temperature at which a measurable rate is detected) for iodine loaded samples follows this order: $C_{12}H_{25}I$ (493.6°C) ≈ I_2 (481.0°C) > C_4H_9I (454.3°C) > CH_3I (426.5°C). This information suggests that iodine adsorbed in different samples has different thermal stability, which, in turn, indicates that there might be different forms of iodine species formed. For instance, previous studies proved the coexistence of α- and γ- AgI in I_2 and CH_3I loaded Ag^0Z.[8, 9] γ-AgI is distributed on the mordenite surface as nanoparticles, while α-AgI forms within the mordenite channels. α-AgI is formed at sub-nanometer sizes and cannot be detected by XRD. Future characterization will focus on probing the predominant phase of AgI and further evaluating the volatile species in the samples.

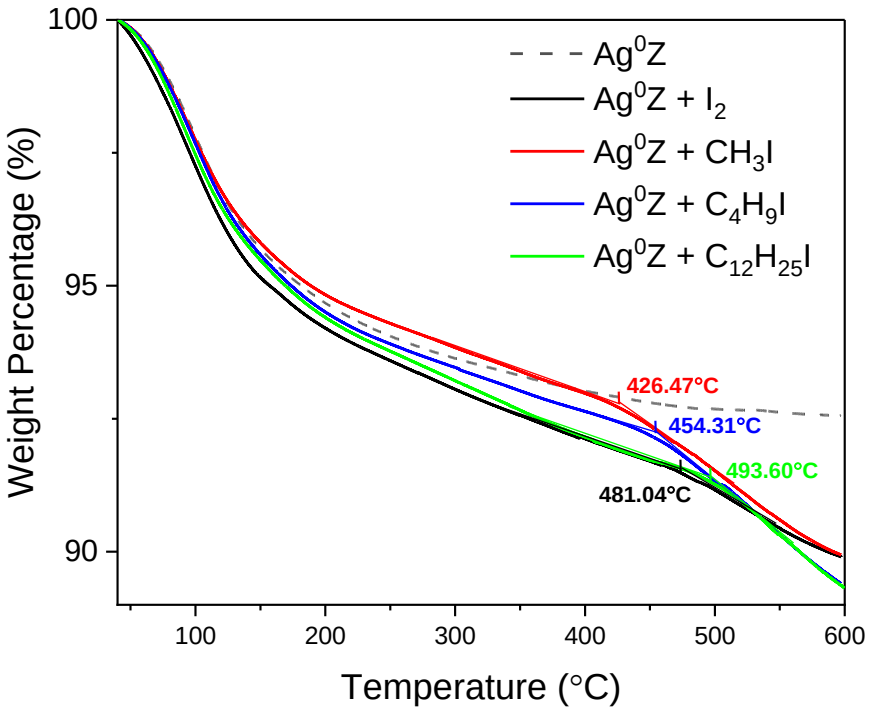

Figure 4. TGA curves for pristine Ag^0Z and Ag^0Z loaded with CH_3I, C_4H_9I, $C_{12}H_{25}I$, and I_2; for each sample, the onset temperatures that indicate iodine release are labeled.

1.4 Conclusions

The capture performance of alkyl iodides with different carbon chain lengths was reported in previous studies, but the underlying mechanisms governing these adsorption processes have not yet been evaluated. Although *in situ* characterization for the adsorbents and outlet gas during the adsorption processes can usually provide more in-depth mechanistic information,[10] previous research demonstrated that *ex situ* analysis on the iodine loaded adsorbents could also serve as a promising tool to unravel the underlying processes occurring in the adsorption processes.[8] In this study, SEM-EDX, PXRD, UV-vis DRS, and TGA analyses were performed to examine the physical and chemical properties of Ag^0Z loaded with different iodine species. These preliminary investigations suggest that AgI is the predominant adsorption product regardless of the adsorbed iodine species, yet slight deviations may be present in the AgI phases. For instance, alkyl iodides with longer carbon chain length may have a different composition of α- and γ-AgI. To quantify these two AgI phases, synchrotron pair distribution function (PDF) measurements have been conducted at beamline 11-ID-B in the Advanced Photon Source (APS) at Argonne National Laboratory. In addition, TGA coupled with a Fourier transformed infrared detector (TGA-FTIR) was also conducted to evaluate the volatile species in iodine loaded samples. These results may provide further insights into the capture mechanisms and will be discussed in the project final report.

Part 2: Fixed-Bed Simulations for CH_3I Adsorption on Ag^0Z

Key Personnel

Ziheng Shen (Ph.D. Student), Austin Ladshaw (Former Ph.D. Student), Alexander Wiechert (Postdoc), Costas Tsouris (Co-PI), Sotira Yiacoumi (PI)

2.1 Scope

The primary objective of computational simulations is to establish a scalable adsorption model that enables accurate prediction of column performance for silver-based adsorbents used in the capture of organic iodides. To accomplish this goal, a clear understanding of the uptake processes is required. According to Greaney et al., a distinct shrinking-core process was observed in the adsorption processes for all the iodine species, which indicates that the uptake mechanisms may involve both transport (gas film diffusion and pore diffusion) and chemical reaction processes. In this section, the feasibility of using computational tools to simulate the CH_3I adsorption performance in both thin-bed and deep-bed columns is discussed.

2.2 Modeling Methodology

In general, the equations for modeling fixed-bed column adsorption are derived from the gas-phase mass-conservation equations. The entire process was considered isothermal such that the energy conservation was not involved in the modeling. In a packed column, for instance, the adsorption of CH_3I onto Ag^0Z can be described as a combination of a macroscale (i.e., in the bulk phase of the bed) and a microscale (i.e., in the pellets) mass conservation. Macroscale mass accumulation for CH_3I (Equation 1) is based on the concentration of CH_3I in the bulk phase (C_{b,CH_3I}) and the bulk bed porosity (ε_b) which defines the void space where gas may exist. The gas mixture can move in the void space of the column through advection (at an advective velocity of v) and dispersion (with a dispersion coefficient of D_b) transport mechanisms. CH_3I in the bulk phase will transfer into the pellet (pore space) with a mass transfer coefficient k_m; note that the specific-area term (G_a) represents exposed surface area per total reactor volume. The pellet is simplified to be spherical in shape (at an equivalent diameter of 0.18 mm), and the mass conservation (Equation 2) is dependent on the pore-space concentration (C_{p,CH_3I}), pellet porosity (ε_p), and intraparticle pore diffusivity of CH_3I (D_p). Specifically, the advection term is not included in the pore-space.

$$\varepsilon_b \frac{\partial C_{b,CH_3I}}{\partial t} + \nabla \cdot \left(\varepsilon_b v C_{b,CH_3I}\right) = \nabla \cdot \left(\varepsilon_b D_b \nabla C_{b,CH_3I}\right) - (1-\varepsilon_b) G_a k_m (C_{b,CH_3I} - C_{p,CH_3I}) \quad (1)$$

$$r^2 \varepsilon_p (1-\varepsilon_b) \frac{\partial C_{p,CH_3I}}{\partial t} = \frac{\partial}{\partial r} \cdot \left(r^2 \varepsilon_p (1-\varepsilon_b) D_p \frac{\partial C_{p,CH_3I}}{\partial r} \right) - r^2 (1-\varepsilon_b) r_{CH_3I} \quad (2)$$

Preliminary analysis on iodine loaded samples, as discussed in Part 1, suggests that the final adsorption products are likely γ-AgI and α-AgI for all the iodine-loaded samples. For simplicity, Equation 3 was assumed to be an overall representation of the adsorption reaction between available Ag sites (Ag^*) and CH_3I although more complex catalytic reactions for CH_3I adsorption onto Ag^0Z have been proposed by other researchers.[8] Adsorption would represent a

loss to the gas phase within the pellet based on the net adsorption rate (r_{CH_3I}), defined by the reaction rate constant k_f (Equation 4). Since Equation 4 is derived based on a simplified reaction, the order of reaction may not follow the reaction stoichiometry; the power with respect to Ag^0 (n) was, therefore, adjusted to provide a reasonable description of the data. The concentration of Ag sites and AgI in the pellet phase follows the material balance described as Equation 5, where q_{max} is a fixed value calculated based on the Ag content of a pristine Ag^0Z pellet. The initial condition and boundary conditions are expressed by Equations 6-8. Physical properties in the equations (ε_b, G_a, etc.) can be directly measured or calculated, and the gas film mass transfer coefficient k_m was estimated based on empirical equations reported in the literature.[11]

$$Ag^* + CH_3I \xrightarrow{k_f} AgI + CH_3^* \tag{3}$$

$$r_{CH_3I} = k_f q_{Ag^*}^n \times C_{p,CH_3I} \tag{4}$$

$$q_{Ag^*} + q_{AgI} = q_{max} \tag{5}$$

$$C_{p,CH_3I} = 0, @\ t = 0,\ 0 \le r \le r_p \tag{6}$$

$$\frac{\partial C_{p,CH_3I}}{\partial r} = 0, @\ r = 0 \tag{7}$$

$$\varepsilon_p(1-\varepsilon_b)D_p \frac{\partial C_{p,CH_3I}}{\partial r} = k_m(C_{b,CH_3I} - C_{p,CH_3I|r=r_p}), @r = r_p \tag{8}$$

These differential equations were solved using the Catalysis And Treatment System (CATS) modeling framework,[12] which is an upgraded version of the Discontinuous Galerkin Off-gas Separation and Recovery model (DG-OSPREY) framework developed at the Georgia Institute of Technology.[13] CATS is built on top of the Multiphysics Object Oriented Simulation Environment (MOOSE) modeling framework developed at Idaho National Laboratory.[14] The MOOSE framework is designed to handle discretization of spatial domains and iteratively solve non-linear systems of equations. Domain discretization in CATS is performed using the discontinuous Galerkin (DG) method since, in the context of problems derived from conservation laws, it is more stable and less oscillatory than the continuous method.[15, 16] Domain discretization produces a non-linear system of equations which MOOSE solves iteratively using a Preconditioned Jacobian Free-Newton Krylov (PJFNK) method.[17] This method incorporates both a non-linear solver based on Newton type methods and a linear Krylov subspace method which is nested within the non-linear solver, typically the generalized minimal residual (GMRES) method. Convergence of non-linear iterations is controlled using line search methods, such as Back-Tracking.[18] For each linear iteration, preconditioning is performed with incomplete lower and upper triangular fractionalization to improve computational efficiency. Integration in time is carried using either a first-order accurate Backwards Euler method or a second-order accurate Backwards Differentiation method.[19] Compared with its ancestor DG-OSPREY, CATS, itself, offers more modularity in coding and creates more flexibility for users to create the input files.

In the simulations, the reaction rate constant (k_f) and pore diffusivity (D_p) were optimized by fitting the experimental uptake curves of thin-bed tests results. The objective function (Equation

9) was minimized using the Python library LMFIT.[8] Using these values, the breakthrough curve for deep-bed experiments can be predicted.

$$F_{obj} = \sum_{i}^{n} (q_{AgI,i}^{exp} - q_{AgI,i}^{model})^2 \quad (9)$$

2.3 Thin-Bed Description and Deep-Bed Prediction for CH_3I Loading on Ag^0Z

The kinetic parameters (k_f and D_p) were found through optimization and based on the data for thin-bed adsorption experiments. The data used in this study were collected from the annual report prepared by Greaney et al. in FY2021.[5] Specifically, the samples were placed as a thin layer (one to three pellets deep) on a TGA basket with a 2.54 cm circumference. Loading results for CH_3I with two initial concentrations, 5 ppmv and 10 ppmv, were selected for the simulations, and the superficial velocity was 10 m/min for both cases. Using the method reported by Nan et al.,[20] the gas film transfer coefficient k_m was estimated to be 0.98 cm/s. The experimental data and modeling results obtained through optimization are shown in Figure 5. The optimized D_p was 0.0012 cm^2/s, and the adsorption reaction was second order with respect to Ag* with a rate constant k_f of 3.39×10^7 $(mol/g)^{-2}s^{-1}$. The predicted curve describes better the experimental uptake data for 5-ppmv CH_3I, whilst slight deviation at longer periods can be observed in both simulation results. It is hard to ascertain what are the leading attributes to the discrepancies due to the lack of duplicate experiments. The modeling results, however, should sufficiently represent the thin-bed adsorption behavior.

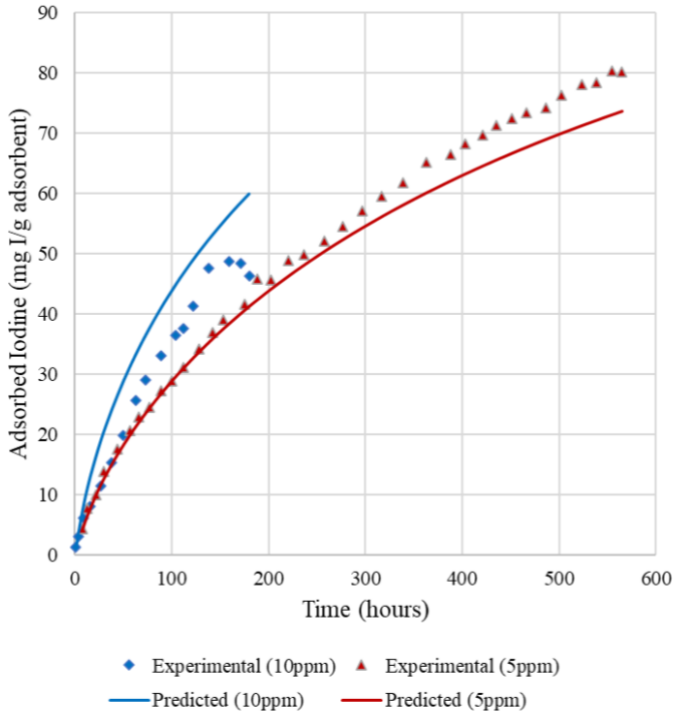

Figure 5. Experimental (dot) and simulated adsorption curves for 10 ppmv (blue) and 5 ppmv (red) CH_3I at a superficial velocity of 10 m/min.

We can then predict the capture performance of CH_3I in a deep-bed Ag^0Z column using the kinetic parameters obtained previously. First, to validate the model, we made a prediction of the adsorption behaviors for 1 ppmv CH_3I on Ag^0Z packed in a 14-cm-depth column with a 2.54-cm inner diameter; two superficial velocities at 1 m/min and 20 m/min were used for the simulations. These conditions were selected because experiments under the same conditions have been conducted and reported previously,[5] and comparing the predicted results to experimental data can reasonably justify the models. Specifically, the period of adsorption was set to be 574 hours for the 1-m/min simulation and 28 hours for the 20-m/min one, which strictly followed the actual experimental conditions.

Predicted and experimental CH_3I penetration profiles are demonstrated in Figure 6; we must note that the experimental values were determined by measuring the average iodine loading in each subsection of the bed after the loading was completed. In both simulation cases, the predicted profiles slightly underestimated the amount of iodine captured at all depths in the bed. For the 20-m/min-velocity simulation, specifically, the predicted uptake values were only ~60% of the experimental ones. The qualitative conclusions are, however, very consistent between the predicted and experimental data. For instance, the models successfully predicts that the penetration depth for the 1 m/min CH_3I is ~6 cm after 574 hours, and that the 20-m/min CH_3I gas stream penetrates throughout the 14-cm bed after 28 hours. The underestimation may come from the discrepancies in the parameters describing the thin bed loading which, as discussed before, still lack a promising explanation. Some plausible factors include the potential competing effect of H_2O co-adsorption (2 ppmv H_2O was present in the carrier gas); this effect may be more pronounced in a deep-bed experiment. In addition, the CH_3I concentration used in the deep-bed experiments (1 ppmv) was lower than that in the thin-bed experiments (5 and 10 ppmv), which may slightly alter the rates of transport. Furthermore, because the thin-bed experiments were conducted on a TGA plate whereas deep-bed ones were performed in a column, there might be a deviation in packing (e.g., different bed porosities).

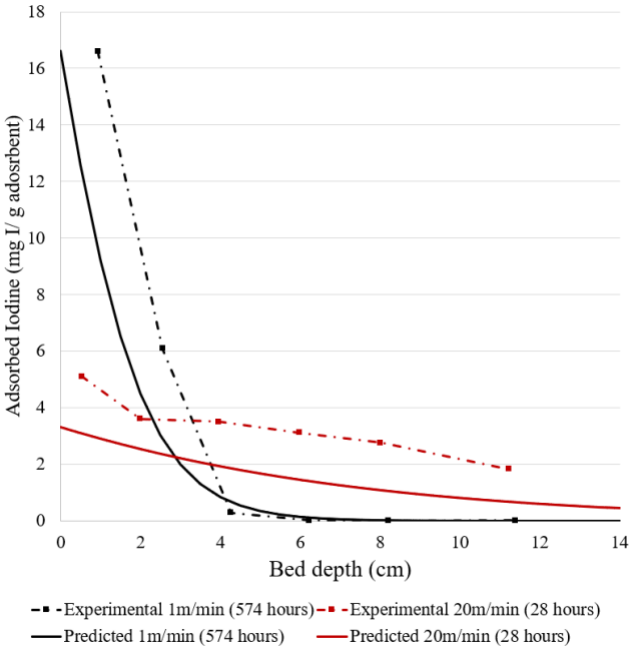

Figure 6. Penetration profiles for 1 ppmv CH_3I at 1-m/min superficial velocity with 574-h loading period (black) and 20-m/min superficial velocity with 28-h loading period (red); both experimental (dots) and simulated results (solid lines) are presented for comparison.

To improve the prediction accuracy for a deep bed, we may focus on obtaining a better modeling description of the thin bed experiments and, meanwhile, obtain more precise values for the parameters that describe the deep bed system. Approaches include, for instance, using only the 5-ppm thin-bed experimental data, accounting for the co-adsorption of H_2O, e.g., multicomponent adsorption modeling, to find through optimization the gas film transfer coefficient (k_m; the current value was calculated based on empirical equations). We also need to point out that the sample inhomogeneity may also contribute to the uncertainties in the experimental loading curve, and duplicate experiments are suggested to be conducted. Despite the slight underestimation in the penetration profiles, the perfect match in the penetration depth suggests the models have good capabilities in predicting the behavior of deep beds.

We further predict the breakthrough curves for 1-ppmv CH_3I loaded on bed at 1, 5, 10, and 20 m/min (Figure 7). Results indicate that when the superficial velocity is 20 m/min, breakthrough (defined as $C_e/C_0 = 0.05$, where C_0 denotes the CH_3I concentration of the inlet stream, and C_e denotes the CH_3I concentration at the outlet) occurred immediately after adsorption commenced making it an unviable option. Based on the actual design requirements, velocities under 10 m/min shall be acceptable. Such prediction results well complement the experimental studies, given that the experimental settings were not capable of real-time monitoring of the outlet concentrations. The models can also provide guidance for more complex process designs.

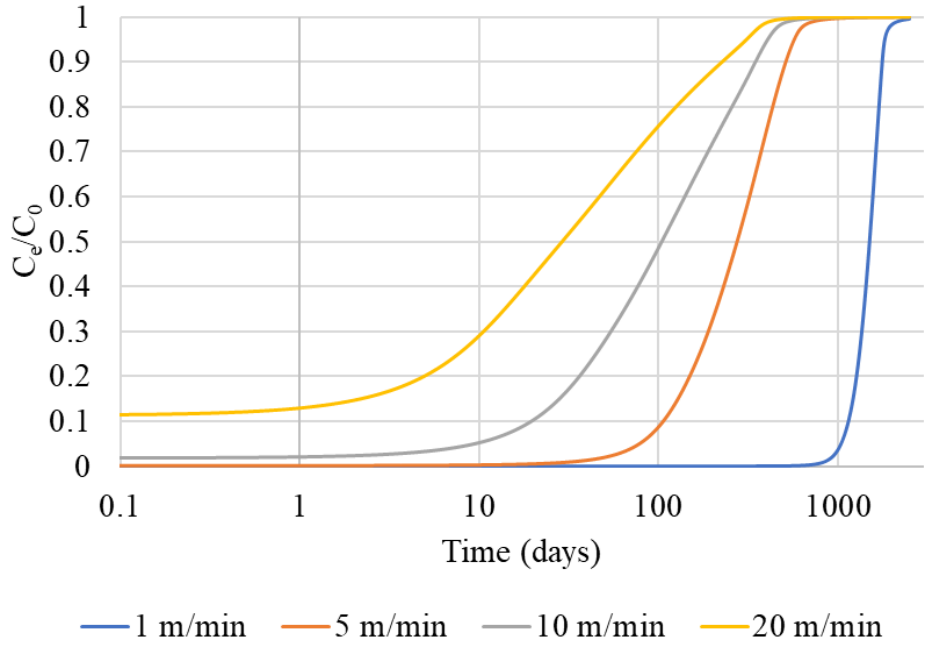

Figure 7. Predicted breakthrough curves for 1-ppmv CH_3I at superficial velocities of 1, 5, 10, and 20 m/min. C_0 denotes the CH_3I concentration of the inlet stream, and C_e denotes the CH_3I concentration at the outlet.

2.5 Conclusions

Fixed-bed models were successfully implemented to predict the deep-bed adsorption performance including the penetration profiles and breakthrough curves. Some discrepancies were observed between the simulation results and experimental data. The primary focus in future studies will be, as discussed in Section 2.4, to improve the modeling description of thin beds in order to obtain more accurate predictions of deep beds. In addition, the thin-bed experimental data for other iodine species (I_2, C_4H_9I, and $C_{12}H_{25}I$) may also be described through optimization using the mechanistic model discussed in this work, and then the corresponding deep-bed performance may be predicted.

References:

(1) Chebbi, M.; Azambre, B.; Volkringer, C.; Loiseau, T. Dynamic sorption properties of Metal-Organic Frameworks for the capture of methyl iodide. *Microporous and Mesoporous Materials* **2018**, *259*, 244-254. DOI: 10.1016/j.micromeso.2017.10.018.

(2) Riley, B. J.; Vienna, J. D.; Strachan, D. M.; McCloy, J. S.; Jerden, J. L. Materials and Processes for the Effective Capture and Immobilization of Radioiodine: A Review. *Journal of Nuclear Materials* **2016**, *470*, 307-326. DOI: 10.1016/j.jnucmat.2015.11.038.

(3) Chibani, S.; Chebbi, M.; Lebègue, S.; Bučko, T.; Badawi, M. A DFT Investigation of the Adsorption of Iodine Compounds and Water in H-, Na-, Ag-, and Cu-mordenite. *The Journal of chemical physics* **2016**, *144* (24), 244705.

(4) Greaney, A. T.; Bruffey, S. H. *Comparison of Extended and Accelerated VOG Tests*; Oak Ridge National Lab.(ORNL), Oak Ridge, TN (United States), 2020.

(5) Greaney, A.; Bruffey, S.; Soelberg, N.; Welty, A. K. *Organic Iodide Adsorption from Dilute Gas Streams*; Oak Ridge National Lab.(ORNL), Oak Ridge, TN (United States), 2021.

(6) Azambre, B.; Chebbi, M.; Ibrahim, N. Structure-Activity Relationships between the State of Silver on Different Supports and Their I_2 and CH3I Adsorption Properties. *Nanomaterials (Basel)* **2021**, *11* (5). DOI: 10.3390/nano11051300 From NLM PubMed-not-MEDLINE.

(7) Aspromonte, S. G.; Mizrahi, M. D.; Schneeberger, F. A.; López, J. M. R.; Boix, A. V. Study of the Nature and Location of Silver in Ag-Exchanged Mordenite Catalysts. Characterization by Spectroscopic Techniques. *The Journal of Physical Chemistry C* **2013**, *117* (48), 25433-25442. DOI: 10.1021/jp4046269.

(8) Nenoff, T. M.; Rodriguez, M. A.; Soelberg, N. R.; Chapman, K. W. Silver-mordenite for Radiologic Gas Capture from Complex Streams: Dual Catalytic CH_3I Decomposition and I Confinement. *Microporous and mesoporous materials* **2014**, *200*, 297-303. DOI: 10.1016/j.micromeso.2014.04.041.

(9) Chapman, K. W.; Chupas, P. J.; Nenoff, T. M. Radioactive Iodine Capture in Silver-Containing Mordenites through Nanoscale Silver Iodide Formation. *Journal of the American Chemical Society* **2010**, *132* (26), 8897-+. DOI: 10.1021/ja103110y.

(10) Chebbi, M.; Azambre, B.; Cantrel, L.; Koch, A. A Combined DRIFTS and DR-UV–Vis Spectroscopic In Situ Study on the Trapping of CH3I by Silver-Exchanged Faujasite

Zeolite. *The Journal of Physical Chemistry C* **2016**, *120* (33), 18694-18706. DOI: 10.1021/acs.jpcc.6b07112.

(11) Tang, S.; Choi, S.; Nan, Y.; Tavlarides, L. L. Adsorption of Methyl Iodide on Reduced Silver-functionalized Silica Aerogel: Kinetics and Modeling. *AIChE Journal* **2021**, *67* (4), e17137. DOI: 10.1002/aic.17137.

(12) Ladshaw, A.P., "CATS: Catalysis And Treatment Systems -- MOOSE based catalysis simulation tool," https://github.com/aladshaw3/cats

(13) Ladshaw, A. P.; Wiechert, A. I.; Welty, A. K.; Lyon, K. L.; Law, J. D.; Jubin, R. T.; Tsouris, C.; Yiacoumi, S. Adsorbents and Adsorption Models for Capture of Kr and Xe Gas Mixtures in Fixed-bed Columns. *Chemical Engineering Journal* **2019**, *375*, 122073.

(14) Gaston, D.; Newman, C.; Hansen, G.; Lebrun-Grandie, D. MOOSE: A Parallel Computational Framework for Coupled Systems of Nonlinear Equations. *Nuclear Engineering and Design* **2009**, *239* (10), 1768-1778.

(15) Houston, P.; Schwab, C.; Süli, E. Discontinuous hp-finite Element Methods for Advection-diffusion-reaction Problems. *SIAM Journal on Numerical Analysis* **2002**, *39* (6), 2133-2163.

(16) Riviere, B. *Discontinuous Galerkin methods for solving elliptic and parabolic equations: theory and implementation*; SIAM, 2008.

(17) Knoll, D. A.; Keyes, D. E. Jacobian-free Newton–Krylov methods: a survey of approaches and applications. *Journal of Computational Physics* **2004**, *193* (2), 357-397.

(18) Eckert, S.; Baaser, H.; Gross, D.; Scherf, O. A BDF2 Integration Method with Step Size Control for Elasto-plasticity. *Computational Mechanics* **2004**, *34* (5), 377-386.

(19) Dennis Jr, J. E.; Schnabel, R. B. *Numerical Methods for Unconstrained Optimization and Nonlinear Equations*; SIAM, 1996.

(20) Nan, Y.; Tavlarides, L. L.; DePaoli, D. W. Adsorption of Iodine on Hydrogen-reduced Silver-exchanged Mordenite: Experiments and Modeling. *AIChE Journal* **2017**, *63* (3), 1024-1035. DOI: 10.1002/aic.15432.